ACS APPLIED MATERIALS & INTERFACES

Research Article

www.acsami.org

Three Dimensional Indium–Tin-Oxide Nanorod Array for Charge Collection in Dye-Sensitized Solar Cells

Byunghong Lee,[†,‡,§] Peijun Guo,[†,‡,§] Shi-Qiang Li,[†,‡] D. Bruce Buchholz,[†,‡] and Robert P. H. Chang*[,†,‡]

[†]Department of Materials Science and Engineering, [‡]Materials Research Institute, Northwestern University, 2220 Campus Drive, Evanston, Illinois 60208, United States

ABSTRACT: In this article, we report the design, fabrication, characterization, and simulation of three-dimensional (3D) dye-sensitized solar cells (DSSCs), using ordered indium–tin-oxide (ITO) nanorod (NR) arrays as the photoanode, and compare them with conventional planar (2D) DSSCs. The ITO NR array used in the 3D cell greatly improves its performance by providing shorter electron pathways and reducing the recombination rate of the photogenerated electrons. We observed a 10–20% enhancement of the energy conversion efficiency, primarily due to an increased short circuit current. This finding supports the concept of using 3D photoanodes with optically transparent and conducting nanorods for the enhancement of the energy-harvesting devices that require short charge collection distance without sacrificing the optical thickness. Thus, unlike the conventional solar cell structure, the functions for photon collection and charge transport are decoupled to allow for improved cell designs.

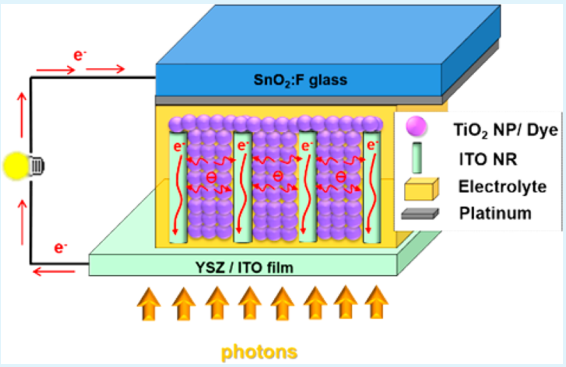

KEYWORDS: *dye sensitized solar cell, indium–tin-oxide nanorod, charge collection, air spray, photonic crystal, finite element modeling*

INTRODUCTION

The next generation of solar cells is currently being developed in the laboratories around the world with a common goal to achieve high efficiency but at much less production cost with environmentally safe materials.[1−3] It is anticipated that these cells can be used in a variety of power generation applications both for outdoors as well as indoors, ranging from window panels to mobile devices. This class of solar cells, currently under research and development include dye-sensitized solar cells (DSSC),[4] organic photovoltaic cells (OPV),[5] quantum dot/rod-based cells (QDC),[6] and hybrids of these cells.[7] Among these, the organic-lead based perovskite cell has recently achieved an efficiency over 15%,[8,9] and with further improvement on the way.

To date most of the solar cell devices are constructed in a planar two-dimensional (2D) geometry, that is, the cells are configured with two parallel planar electrodes, one for light collection and both for charge extraction to the external circuit. The active layers are sandwiched in between for photon-to-charge conversion processes. The efficiency of such a cell, based on its $J-V$ curve is commonly defined by a simple formula, $\eta = J_{sc}V_{oc}FF/P_{in}$, where J_{sc} is the short circuit current, V_{oc} is the open circuit voltage, FF is the fill factor, and P_{in} is the incident power collected by the cell. While all these factors are interconnected, the J_{sc} gives a measure of how efficiently photons are collected and converted to useful charges in the cell, while V_{oc} tells how well the energy levels of the many layers of the cells are aligned to give the optimum and highest value. The bigger challenge is to reduce the internal resistance of the cell due to contributions from charge recombination, traps, and the loss of excitons at the interfaces of the active regions of these cells.[10,11] Thus, to optimize the efficiency of the cell, one needs to collect as many photons as possible, and extract as many charges as possible to the external circuit. The FF of the cell gives a measure of how close it is to the case of an ideal diode. From the $J-V$ curve, it is possible to extract some internal loss information. Of course in a more complicated circuit, there are contributions from the capacitive and inductive elements. A simple requirement to reduce the series resistance of the cell is to have charges move onto the closest conducting path from where they are formed and at the same time to enhance the photon collection capability of the cell. Thus, the ideal cell architecture is one that decouples the functions of photon collection and charge collection. This is the basic concept discussed in the article. An example is given on how a three-dimensional (3D) architecture can help to improve the performance of a conventional DSSC. First, we present and compare 2D and 3D DSSCs' experimental results. To understand the difference in cell performance, simulations are then performed to show why the new 3D architecture is favorable over a 2D geometry.

Cells with planar geometry are easier to fabricate using standard thin film processing techniques. But, how does one decide the thickness of the active layer where photons are

Received: June 26, 2014
Accepted: August 22, 2014
Published: August 22, 2014

captured and converted to charges for transportation to the external circuit? Depending on the type of solar cell, the general approach is to optimize the active layer thickness by balancing between the maximum amount of photons absorbed and the maximum amount of charges transported to the external circuit.[12−14] To this end, the optimal thickness reflects the case for which the cell achieves the overall highest efficiency. Thus, the key concept in the 3D architecture design is to minimize the resistive contribution from the active region by having charges spend much less time there before traveling to the outside circuit, but at the same time maintaining or improving the photon collection.

Figure 1 illustrates the operational principle of a conventional DSSC consisting of a pair of electrodes (anode and cathode)

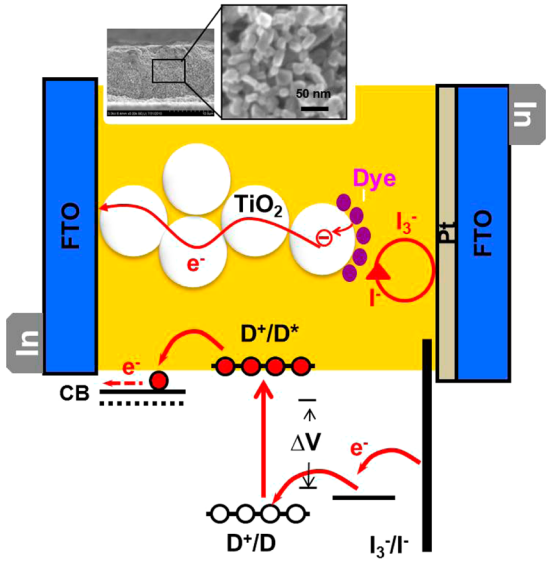

Figure 1. Schematic diagram and principle of operation of dye-sensitized solar cells. (Image is reproduced with permission from ref 12, copyright American Chemical Society).

with the active layer (photon-to-charge conversion) sandwiched in between. Light enters the DSSC through the transparent conducting anode electrode (left) consisting of a transparent conducting fluorine-doped tin oxide (FTO) substrate with a film of porous TiO_2 nanoparticles (NPs) coated on top. The TiO_2 NPs in the film are then coated with a monolayer of dye molecules which in turn are soaked in the liquid electrolyte (I^-/I_3^-) for good contact. This liquid electrolyte is also in contact with the cathode (right) consisting of a very thin catalytic layer of Pt on top of a FTO substrate. To optimize the DSSC performance, it is desirable to collect as many photons as possible for a given area or volume. This means the thicker the active (TiO_2 layer), the more photon collection. On the other hand, the charges converted from the photons are transported to the external circuit through a hopping process from one TiO_2 NP to another. Thus, the longer the path length, the higher the probability of losing the charge through recombination at defect sites on the nanocrystal surfaces. The internal resistance to charge flow will increase with increasing active layer thickness. This is illustrated in Figure 2a for data collected from a conventional DSSC cell.[12] It is revealed from the efficiency curve, that the optimal thickness of the active NP layer is about 12 μm for this 2D geometry. It should also be noted that the highest open circuit voltage and fill factor are achieved at the thinnest active layer thickness, while the short circuit current density increases with increasing film thickness (for thickness below 15 μm). In Figure 2b,[12] it is shown that the efficiency per TiO_2 NP increases dramatically as the active NP layer decreases. This shows the large inherent loss of charges in these 2D DSSCs.

To overcome part of the limitations of the 2D cell design, a 3D anode architecture is introduced, where the anode consists of transparent conducting NRs that are evenly inserted into the TiO_2 NP film for efficient charge collection. In this geometry, charges do not have to travel more than half of the NR separation before they are collected and transported to the external circuit. The 3D geometry makes it possible to maintain a large photon collection volume and at the same time minimize the charge collection losses by reducing the distance the charges have to travel before they are collected by the anode electrode, thus, boosting the cell efficiency. It should be noted that the conductivity of the anode electrode is orders of magnitude higher than that of the active layer of the cell.

In the past decade, extensive research efforts have been focused on the development of three-dimensional (3D) architecture DSSCs. For example, TiO_2 nanotube[15] and ZnO nanorod/nanotube[16,17] array-based electrodes have been investigated as efficient photoanodes because they could provide straight channels for photogenerated electrons to

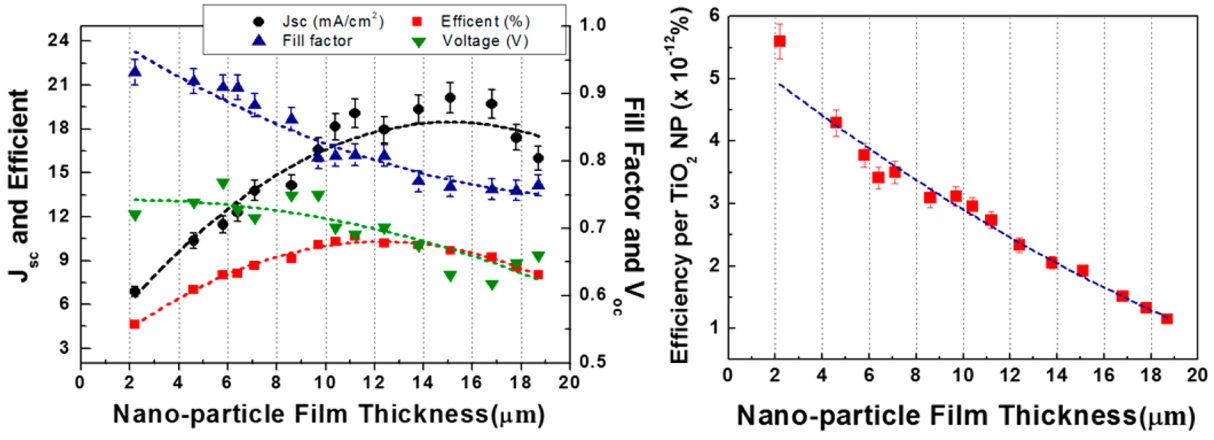

Figure 2. (a) Cell efficiency (in red) versus active layer thickness.[12] (b) Efficiency per nanoparticle versus nanoparticle film thickness.[12] (Images are reproduced with permission from ref 12, copyright American Chemical Society).

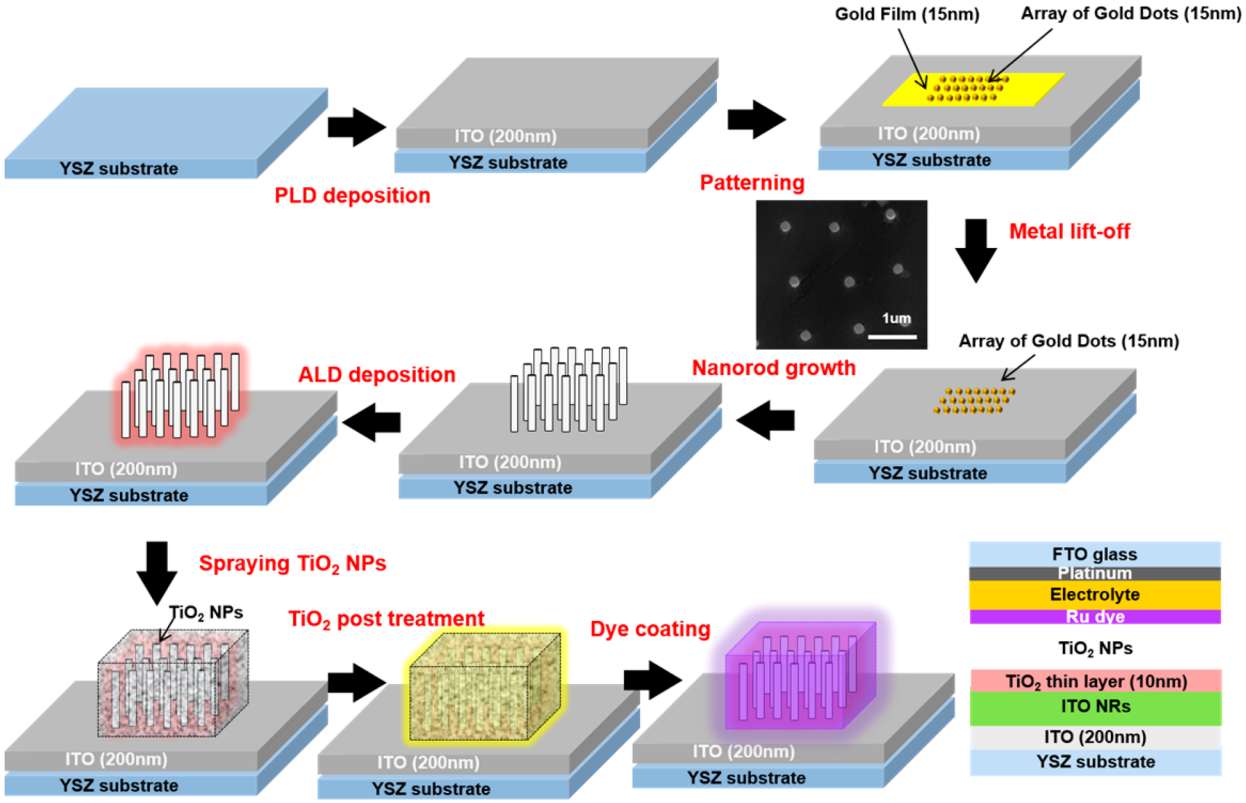

Figure 3. Scheme showing the 3D DSSC (without the counter electrode) fabrication procedure.

reach the contact. Here we revisit the 3D DSSC with ITO NR arrays as part of the conducting anode electrode but not with the semiconducting material used in earlier work. In addition, ZnO is known to degrade in both acidic and basic solutions, and TiO_2 nanotubes have electron mobilities as low as that of TiO_2 NP network, resulting from their exciton-like trap states.[18] Thus, neither ZnO nor TiO_2 may be the ideal 3D conducting channel to prevent charge recombination for efficient DSSCs. Our work is also distinctly different from other works,[19−22] as we relax the charge collection distances from a few nanometers to no more than 2 μm, and simultaneously maintain a high volume density and high surface area of TiO_2 for loading of dye molecules.

EXPERIMENTAL METHODS

To illustrate the effectiveness of the design for the experiments, cubic lattices of ITO NR arrays with 0.6, 1.2 , 2, and 3 μm spacings were studied. The single-crystalline ITO NRs are vertically aligned because they are grown epitaxially from the substrate. We observed that for the 0.6 μm spacing case a complete filling of TiO_2 in the 3D ITO structure without voids is still a challenge. As a result we primarily focused on 1.2, 2, and 3 μm spacings. The ITO NRs were grown using a VLS process,[23] where electron beam lithography was used to pattern seeds of gold NPs on a thin film of ITO grown epitaxially on YSZ using pulsed laser deposition.[24,25] Using the Drude model, the ITO NRs have a calculated resistivity as low as about 1.8×10^{-4} Ω cm, which is in good agreement with published values that were directly measured.[23,26,27] We have also observed that random-distributed ITO NR array, grown vertically on YSZ substrate by a thin layer of gold film as VLS catalyst, worked just as well. Currently, we are also exploring the nanoimprint lithography technique[28] to pattern the gold NP array for high throughput solar cell fabrication.

Figure 3 illustrates the key steps taken to fabricate the 3D anode design with collection NRs distributed throughout to collect charges from the TiO_2 NPs. As a first step, 200 nm thick ITO film was grown on YSZ (100) substrate by pulsed laser deposition method. Following that, a 3% 950 K PMMA in Anisole (950 A3, MicroChem Inc.) was spin-coated on the substrate (4000 rpm, 60 s). Electron beam writing was then performed on FEI Quanta 600F environment SEM to write hole (100 nm in diameter) arrays with selected pitch distance. The exposed sample was subsequently developed in MIBK (methyl isobutyl ketone)/IPA (isopropyl alcohol) 1:3, and titanium (1 nm) and gold films (10 nm) were subsequently deposited by electron beam evaporation (Edward Auto 500; gold shot used is 99.99% trace metal basis from Aldrich; titanium shot is 99.995% trace metal basis from Ted Pella), followed by lift-off in acetone. Through a single-zone quartz-tube furnace, ITO NRs were grown on patterned substrate.[29] A uniform TiO_2 thin layer of thickness of ∼40 nm was deposited on ITO NRs using atomic layer deposition (ALD)[30] with a rate of 0.15 nm per cycle. This layer assures there is no short contact between the ITO NRs and the liquid electrolyte. Vapors of deionized water and titanium tetrachloride ($TiCl_4$, 99.9%, Aldrich) were used as precursors under 0.5 s exposure time and 50 s pumping time, and the substrates were kept at 100 °C. A postannealing treatment at 500 °C for 2 h in ambient condition was performed. Hydrothermal prepared TiO_2 NPs[12,31] were deposited from a spraying method in between the ITO NRs. In the spraying process, the TiO_2 solution was prepared by mixing 10 wt % hydrothermal TiO_2 NPs in 0.1 M acetic acid, 0.05 g polyethylene glycol (PEG, Fluka, Mw = 20,000) and 100 μL of Triton X-100 together. This solution was sprayed using air brush (Speedaire, model 4RR09B) under 40 psi pressure of nitrogen gas. The spray head was situated at a distance of ∼10 cm from the ITO NRs substrates. TiO_2-coated ITO NRs electrode was gradually calcined under an air flow at 150 °C for 15 min, at 320 °C for 10 min, at 500 °C for 30 min. As a post-treatment, a solution of 0.2 M titanium bis(ethyl acetoacetate)diisopropoxide ($C_{18}H_{34}O_8Ti$, Aldrich, 99.9%) in 1-butanol (Aldrich, 99.8%) was coated on ITO NRs/TiO_2 NPs film and sintered at 450 °C for 30 min. The TiO_2 film thickness is made to be 1−2 μm thicker than the ITO NR height, to prevent the ITO NR from contacting the Pt electrode. For photosensitization, the ITO NRs/TiO_2 NP electrode was immersed in ethanol solution containing purified 3×10^{-4} M *cis*-di(thiocyanato)-*N*,*N*′-bis (2,2′-bipyridyl-4-

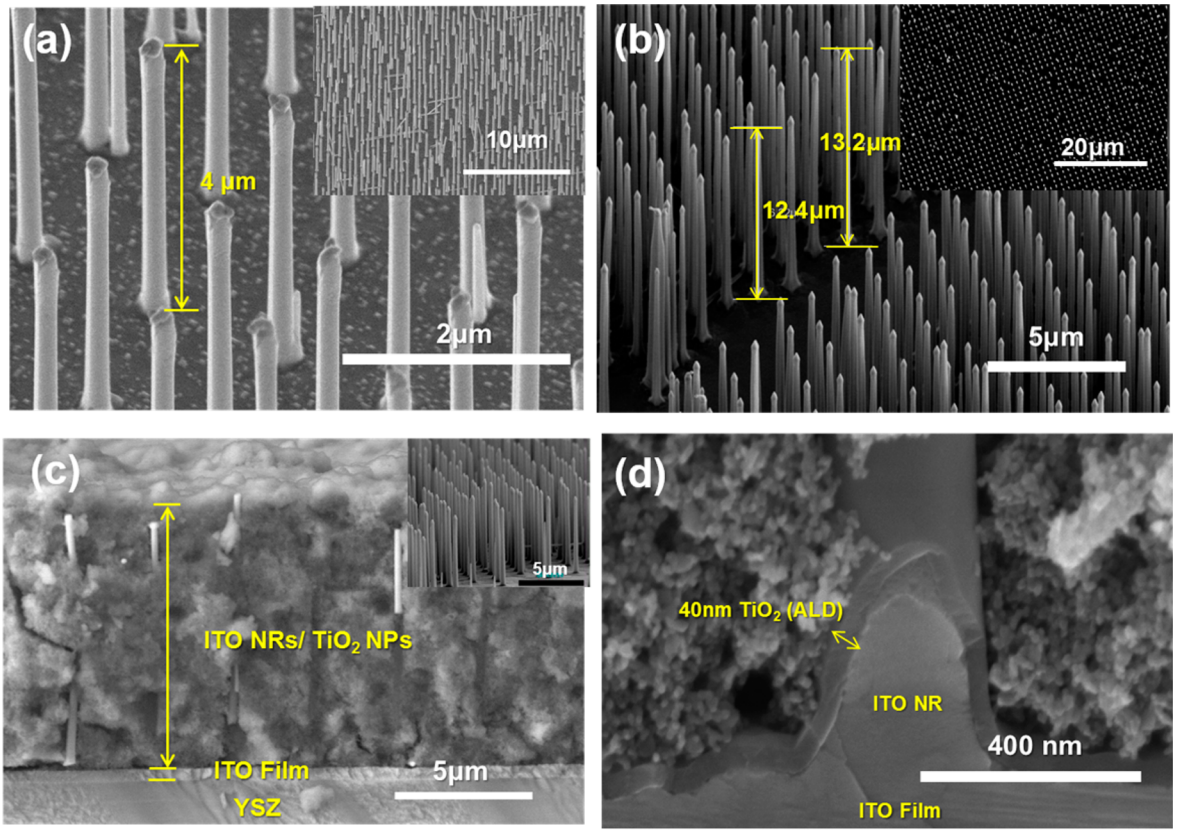

Figure 4. SEM images of well-aligned ITO NRs (inset) infiltrated with TiO_2 NPs. NR spacing is 2 μm in (a) and (d), 1.2 μm in (b), and 3 μm in (c). Viewing angles of (a), (b), and inset of (c) are all 30°. NR height is 4 μm in (a), 13 μm in (b), and 9 μm in (c).

carboxylic acid-4′-tetrabutylammonium carboxylate)ruthenium(II) (N719, Solaronix) for 18 h at room temperature. The liquid electrolyte was prepared by dissolving 0.6 M of 1-butyl-3-methylimidazolium iodide (BMII), 0.03 M of iodine, 0.1 M of guanidinium thiocyanate, and 0.5 M of 4-*tert*-butylpyridine in acetonitrile and valeronitrile (85:15 v/v). The cathode electrode was fabricated by coating FTO glass substrate with a thin layer of a 5 mM solution of H_2PtCl_6 in isopropanol, and it was then heated at 400 °C for 20 min. The two electrodes were sealed together by thermally melting a polymer film (24 μm thick, DuPont).

■ ELECTRICAL MEASUREMENTS

The DSSC devices were evaluated under 100 mW/cm^2 AM1.5G simulated sunlight with a class A solar cell analyzer (Spectra Nova Tech). A silicon solar cell fitted with a KG3 filter tested and certified by the National Renewable Energy Laboratory (NREL) was used for calibration. The KG3 filter accounts for the different light absorption between the dye-sensitized solar cell and the silicon solar cell, and it ensures that the spectral mismatch correction factor approaches unity. A Newport-Oriel IQE-200 ACDC system was used to measure the incident photon to current efficiency (IPCE). The electrochemical impedance spectroscopy (EIS) was measured under the same light illumination with an impedance analyzer (Solartron 1260), and a potentiostat (Solartron 1287) when the device was applied at its V_{oc}. An additional low amplitude modulation sinusoidal voltage of 10 mV rms was also applied between the anode and the cathode of a device over the frequency range of 0.05−150 kHz. The $J-V$ characteristics of the cells were measured using the masked frame method[32] that has been adopted to limit photocurrent over-estimation arising from light-guiding effects that occur as light passes through the conductive glass electrode.

■ RESULTS AND DISCUSSION

Images a and b of Figure 4 show the well-aligned ITO NRs. Figure 4c shows how well the TiO_2 NPs have infiltrated among the ITO NRs. The voids in Figure 4c are the result of cleaving the sample for SEM imaging. A closer look at the interface between the ITO NR and the TiO_2 in Figure 4d shows that there is room for interfacial connectivity improvement.

Preliminary data comparing a 2D cell with a 3D cell show an improvement in efficiency in the range of 10−20%. No difference was observed among the 3D DSSCs with 1.2, 2, and 3 μm spaced ITO NR arrays. The reason for this is that the half-distance between the ITO nanorods are all less than 2 μm which is the lowest value in Figure 2 for separation. Extensive data have been collected to demonstrate accuracy and reproducibility. These results have demonstrated one of the highest efficiencies to date with N719 dye, and it has also substantiated the concept behind the unique 3D architecture. Figure 5a shows $J-V$ curves of the 2D and 3D DSSC with different thicknesses. Their performances are summarized in Table 1. The J_{sc} is found to increase with the film thickness, and an enhancement of the J_{sc} is achieved by the 3D DSSC over the 2D DSSC. Especially, in the case of 3D DSSC with TiO_2 film thicknesses of 5, 10, and 15 μm, the efficiency (η) enhancements are about 11.8%, 13.3%, and 17.2% for the DSSC without using photonic crystals for photon confinement, and are about 17.1%, 18.5% and 20.0% for the DSSCs using photonic crystals, compared to that of the 2D-DSSC, respectively. As the total TiO_2 film thickness increases (i.e, as

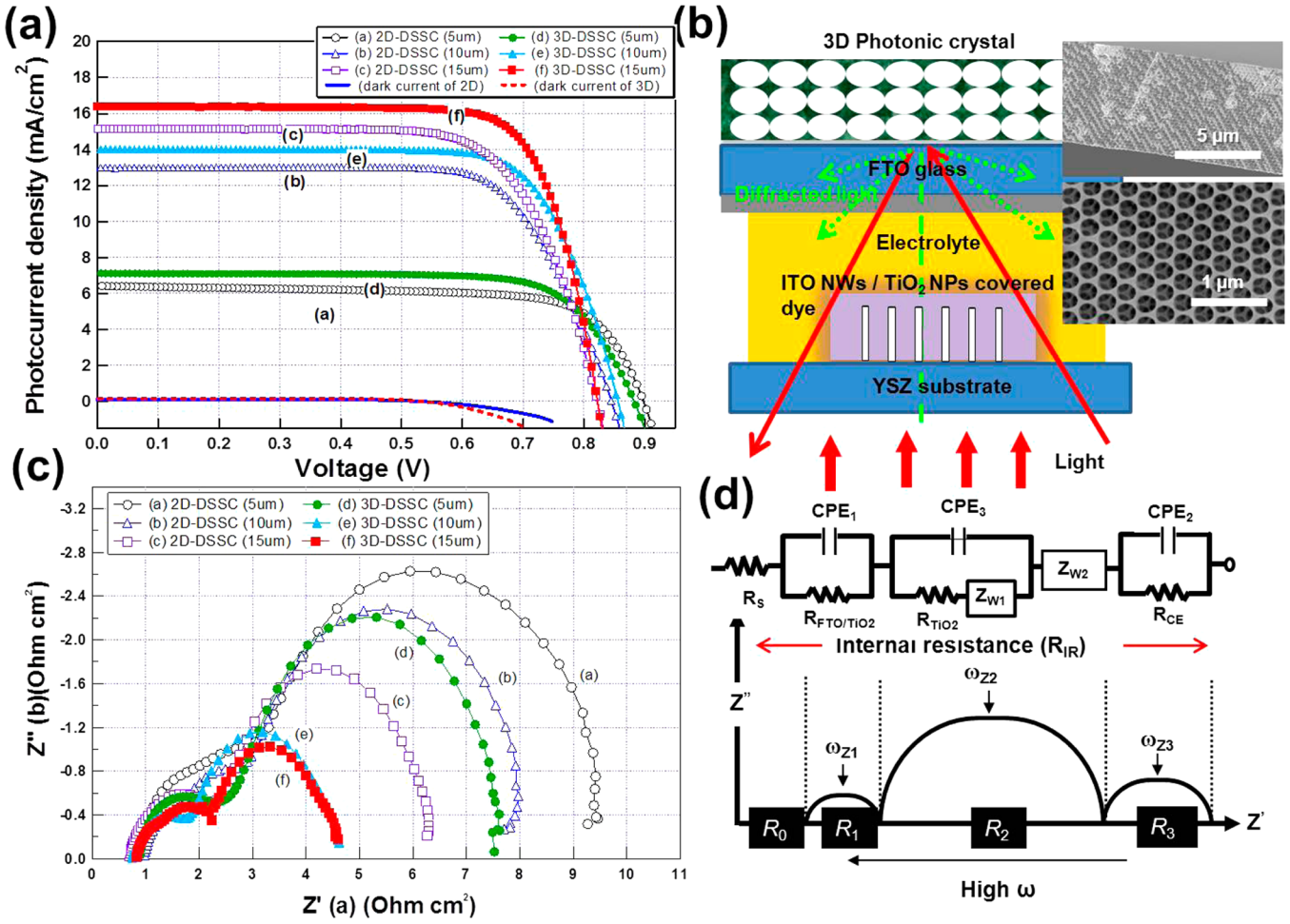

Figure 5. (a) *J*–*V* characteristics of the 3D architecture DSSC (without photonic crystals). (b) Schematic of a 3D DSSC with wave optics (3D photonic crystals) to trap light with reflection and diffraction. (c) Nyquist plot and (d) equivalent circuit of 2D and 3D DSSC (without photonic crystals).

Table 1. Results of EIS and *JV* Characteristics of the 2D and 3D DSSC

			JV characteristics									
			w/o 3D photonic crystals						w 3D photonic crystals			
DSSC type	total thickness (ITO NR height for 3D DSSCs)	area (cm^2)	V_{oc} (V)	J_{sc} (mA/cm^2)	*FF* (-%)	*EFF* (%)	R_{TiO2} (Ωcm^2)	R_{IR} (Ωcm^2)	V_{oc} (V)	J_{sc} (mA/cm^2)	*FF* (%)	*EFF* (%)
2D	≈ 5	0.235	0.898	6.41	72.3	4.16	6.93	9.61	0.891	7.46	71.9	4.78
	≈ 10	0.286	0.845	12.96	71.4	7.82	5.58	8.24	0.838	15.03	71.7	9.03
	≈ 15	0.201	0.822	15.1	70.6	8.79	3.91	6.35	0.823	17.55	69.1	9.98
3D	≈ 5 (4)	0.201	0.883	7.12	74.0	4.65	5.09	7.70	0.882	8.62	73.6	5.60
	≈ 10 (9)	0.212	0.856	14.0	74.0	8.86	2.65	4.58	0.860	16.9	73.2	10.7
	≈ 15 (13)	0.201	0.821	16.3	76.2	10.3	2.28	4.56	0.822	18.4	75.8	11.5

the ITO NRs become longer), the enhancement of the conversion efficiency of 3D DSSCs has also increased, due to a more significant improvement of the short circuit current. The enhanced photocurrent of 3D DSSC is attributed to their lower series resistance that facilitates photogenerated carrier transport. However, we note that it is more difficult to have complete filling of the TiO_2 NPs and a concurrent dye loading density into the gap between ITO NRs as the NR height increases,[33] and a more careful study is currently underway. In general, J_{sc} can be approximated by the expression; $J_{sc} = q\eta_{lh}\eta_{inj}\eta_{cc}I_0$, where q is the elementary charge, η_{lh} is the light-harvesting efficiency of a cell, η_{inj} is the charge-injection efficiency, η_{cc} is charge collection efficiency, and I_0 is the incident photon flux.[34] We assume that η_{lh} and η_{inj} values from adsorbed N719 dye of 2D and 3D DSSC are similar for all the samples with different thicknesses. We can conclude that the higher J_{sc} and η of 3D DSSC are due to improved η_{cc} value determined by the competition between recombination and charge collection.[34,35]

The effect on the internal charge transport can be obtained by EIS measurements. The detailed internal series resistance (R_{IR}) are summarized in Table 1. The internal series resistance elements are related to the sheet resistance of FTO (R_0), the charge transfer processes at the counter electrode (R_1), the

dx.doi.org/10.1021/am504126g | ACS Appl. Mater. Interfaces 2014, 6, 17713–17722

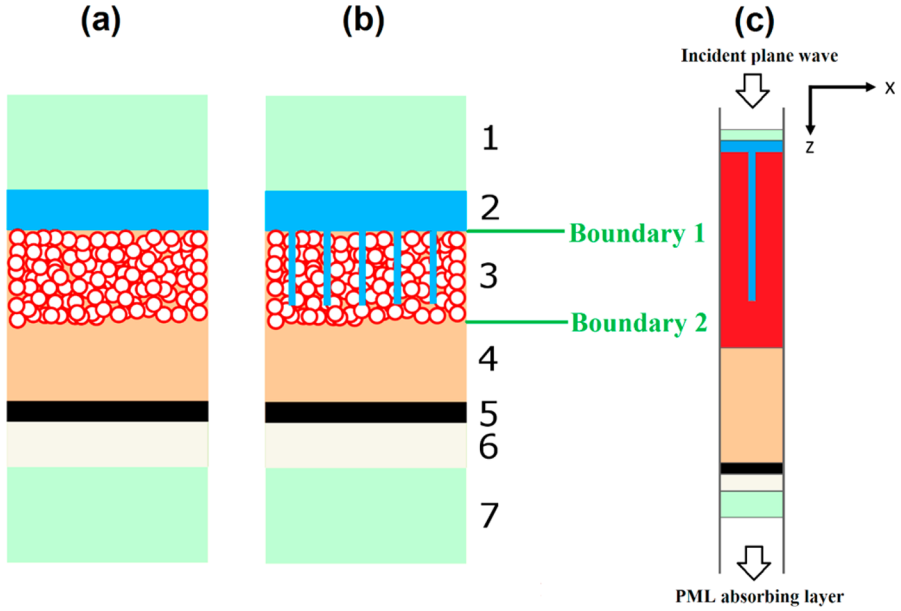

Figure 6. Illustration of the 2D (a) and 3D DSSC structure (b), and the optical simulation setup (c). (Layers: (1) YSZ substrate; (2) ITO film in (a), ITO film and ITO NR in (b); (3) TiO_2 nanoparticles attached with dye molecules, mixed with electrolyte; (4) electrolyte; (5) Pt layer; (6) FTO layer; (7) glass substrate.) In (c), the wave is launched from the top with the k vector along the z direction and polarization along the x direction.

charge transportation at the TiO_2/dye/electrolyte interface (R_2), diffusion in the electrolyte (R_3). As solar cells generally operate under direct current conditions, the capacitances can be ignored. The R_{IR} can then be described as $R_{IR} = R_0 + R_1 + R_2 + R_3$, which for 3D DSSC is significantly lower than that of 2D DSSC (see Figure 5c). The decreased value of R_{IR} of 3D DSSC at the interface between TiO_2/dye/electrolyte interface (R_2) would result in small energy loss for electron transfer and thus photocurrent density enhancement.

Figure 5b illustrates the configuration of the cell with the 3D photonic crystals. As discussed in our earlier work,[12,31] the overall cell efficiency can be increased by as much as 12% using a 3D photonic crystal layer (based on wave optics) and can efficiently reflect and diffract the transmitted photons back into the cell. Therefore, the optimized 3D architecture DSSC with 3D PC gives a J_{sc} of 18.4 mA/cm^2, V_{oc} of 0.822 V, FF of 75.8%, and η of 11.5%. It is anticipated that one can reach 15% by a choice of improved dye molecules and electrolytes.[36]

SIMULATION

In this section we perform numerical simulation to study the coupled optical and electrical properties of a generic DSSC for the 2D and 3D constructions. The simulation is based on a finite element method (FEM) enabled by COMSOL Multiphysics, which is capable of studying coupled physics problems. We discuss the procedures and results of the FEM modeling and elucidate the key performance advantages of the 3D electrode design over that of the 2D geometry.

The FEM model developed in this work is a two-step, interconnected, coupled optical−electrical model. Briefly, in the optical model the explicit Helmholtz electromagnetic wave equation is solved. The generation profile of electrons is calculated from the optical model, and an electron diffusion equation based on the generation profile is then solved in a subsequent electrical model. We note that the advantages of the coupled numerical optical and electrical FEM model include the following. (1) It can solve arbitrary device structures, such as 3D electrode structure used in this work. This 3D structure is beyond the capability of the commonly used Beer−Lambert law for the calculation of optical absorption, and the one-dimensional analytical solution of the electron diffusion equation in planar DSSC.[37,38] (2) FEM can mesh the simulation domain with unstructured grids, so a relatively large structure can be calculated (tens of μm^3 structure is solved in this work), while it cannot be easily handled by the finite difference time domain (FDTD) method. (3) The optical model can take into account the coherence effects due to the layers that are comparable with the wavelength (the ITO film and FTO film), and the incoherence effect due to substrates (the YSZ and glass substrate) that are much thicker than the wavelengths of the incident light. (4) The model is readily capable of studying grating effects and plasmonic effects that will be incorporated into the DSSC structures in our future work. (5) The model is able to generate many useful physical quantities, such as the absorption profile, electron generation profile, recombination profile, and the electron flow paths, and can be postprocessed to render the $J-V$ characteristics, external quantum efficiency and internal quantum efficiency curves, etc.

Figure 6 illustrates the device stack for both 2D and 3D DSSCs, as well as the simulation setup of the model. In the optical model, different layers in the DSSC device stack are represented by their refractive indexes (RIs), respectively. The RI of layer 1, the YSZ substrate, is taken from Sopra Material Database. The RI of layer 2, the ITO film, is fitted by ellipsometry measurement of the ITO film grown on silicon wafer. The RI of the porous TiO_2 medium (layer 3) and the electrolyte (layer 4) are calculated by the Bruggeman effective medium approximation[39,40] based on the published values.[41] The RI of platinum is taken from *Handbook of Optical Constants of Solids* (E. D. Palik).[42] The RI of the fluorine-doped tin oxide (FTO), which is layer 6, is taken from literature.[43] The RI of glass (layer 7) is taken from Sopra Material Database. A plane wave is launched from the top boundary of the simulation domain with its wave vector along the z direction and polarization along the x direction. The total field and scattered field formulation has been used in this work, with details

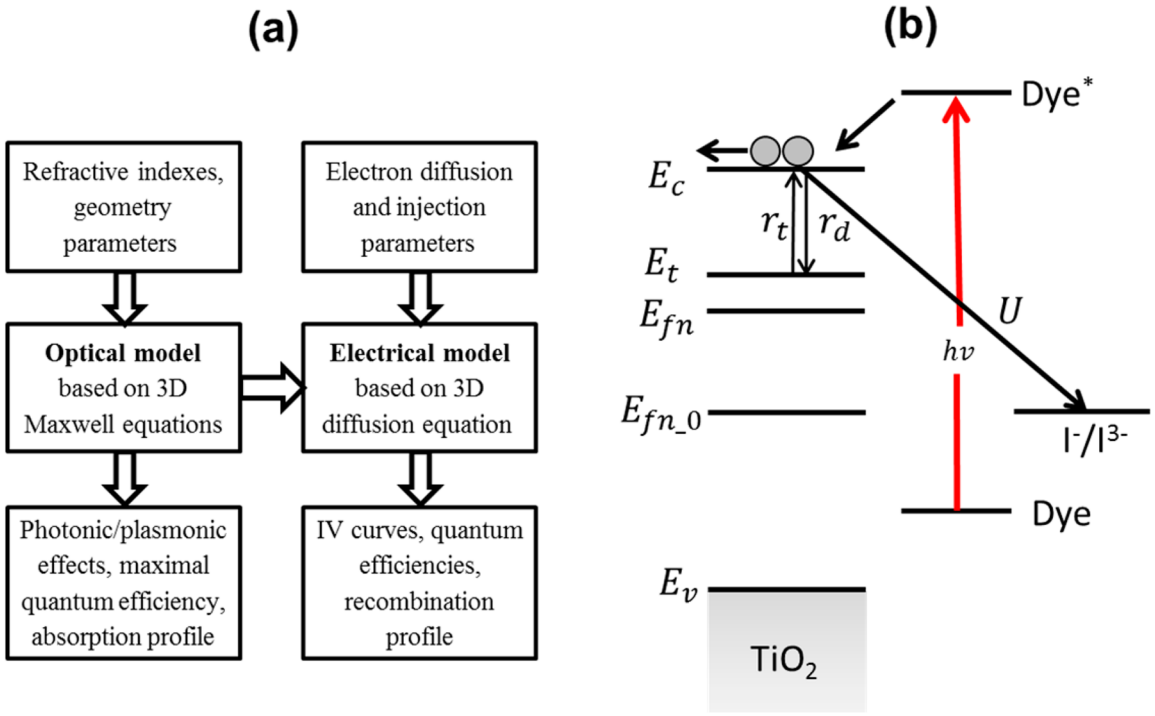

Figure 7. (a) Schematic drawing of the simulation flow; (b) energy diagram and processes considered in the model; E_t is the energy state of the traps, r_t and r_d represent trapping and detrapping rate, respectively.

described in our earlier work.[44] Due to its periodic nature, we reduced the computation domain of the DSSC to a single unit cell. The computational domain is calculated at each wavelength of the solar spectrum within which the N719 dye absorbs, with a wavelength step of 5 nm, and the power of the plane wave at a particular wavelength is determined by the AM 1.5 solar spectrum. The thickness of the YSZ substrate is 0.5 mm, which is much thicker than the wavelength of interest, so the incoherence effect of the YSZ substrate is taken into account by the generalized transfer matrix method.[45] The thickness of the glass on the platinum side is assumed to be infinite, and is terminated by perfectly matched layers (PML), since there is negligible reflection from the glass/interface. We note here that in the model the RI taken from the literatures may not represent the actual devices fabricated in this work, but we argue that this model is intended to qualitatively explain the advantages of the 3D electrode design, so a comparative study of the 2D and 3D DSSCs is still valid as long as the RI for the two cases are kept the same.

In the second step, electron diffusion in the conduction band of TiO_2 is calculated.[37,46] We assume that the electron transport is purely diffusive, so no drift current is considered. This is valid because of the high concentration of ions in the electrolyte which effectively screen the macroscopic electric field. Due to the ill-defined heterogeneous interfaces involved in DSSC operation, the recombination of the electrons in the TiO_2 to oxidized species is complicated and sometimes under debate.[47] However, it is commonly assumed that the main competing process of electron transport through the TiO_2 network is the interception of electrons by I_3^-.[48] A first-order recombination rate with respect to the electron concentration in the TiO_2 conduction band is assumed in this work. Moreover, ionic transport in the electrolyte, as well as the series resistance in the contacts, is not currently included.

The electron diffusion equation used to model the diffusion of electrons within layer 3 (the TiO_2 photoactive layer) in Figure 6 is written as $L^2\nabla^2 n(\vec{r}) - (n(\vec{r}) - \bar{n}) + \tau_0 G(\vec{r}) = 0$. In this diffusion equation, $L = (D\tau)^{1/2}$ is the electron diffusion length in the TiO_2 conduction band, where D is the diffusion coefficient of electrons, and τ is the electron lifetime. $G(\vec{r})$ is the spatial electron generation term that is calculated from the optical model as $G(\vec{r}) = \int(\varepsilon(r)''|E(r)|^2\pi/h)\, d\lambda$, where h is the Planck constant, $E(r)$ is the electric field intensity, and $\varepsilon(r)''$ is the imaginary part of the permittivity of the photoactive layer. At boundary 1, which is the interface between layer 2 (ITO layer) and layer 3 (TiO_2 layer) as shown in Figure 6, the conduction band electron concentration $n_1 = n_0 \exp(eU/k_BT)$ is imposed as the boundary condition. In this equation, U is the photovoltage, n_1 is the conduction band electron concentration, and n_0 is the equilibrium electron concentration in the conduction band of TiO_2 at dark condition, calculated as $n_0 = N_c \exp[-(E_c - E_{fn\_0}/k_BT)]$, where N_c is the effective density of states, taken as 2.5×10^{25} m^{-3},[40] E_c is the conduction band energy, E_{fn_0} is the Fermi level of TiO_2 at dark. $E_c - E_{fn\_0} = E_c - E_{redox}$ is taken to be 1 eV in this work.[46] Different from the 2D DSSC, in 3D DSSC the n_1 constraint is applied to both the planar interface between the TiO_2 and ITO film, as is in the 2D DSSC device, and also at the interface between the TiO_2 and ITO NR surface. At boundary 2 shown in Figure 6, which is the interface between the TiO_2 layer/dye/electrolyte mixture and the electrolyte, the boundary condition $\nabla n_2(\vec{r}) = 0$ is imposed. We choose $L = 10$ μm for the diffusion length,[49,50] and $\tau = 0.5$ ms for both 2D and 3D DSSC simulations.[40] Slight variations of the diffusion length and electron lifetime have resulted in a similar difference between the 2D and 3D DSSCs, and are not shown in this section. An injection efficiency of 0.9, which means that 90% electrons that are in the excited states of the dye will be transferred to the conduction band of TiO_2, is assumed.[40,49] In the current stage of the model, we assume

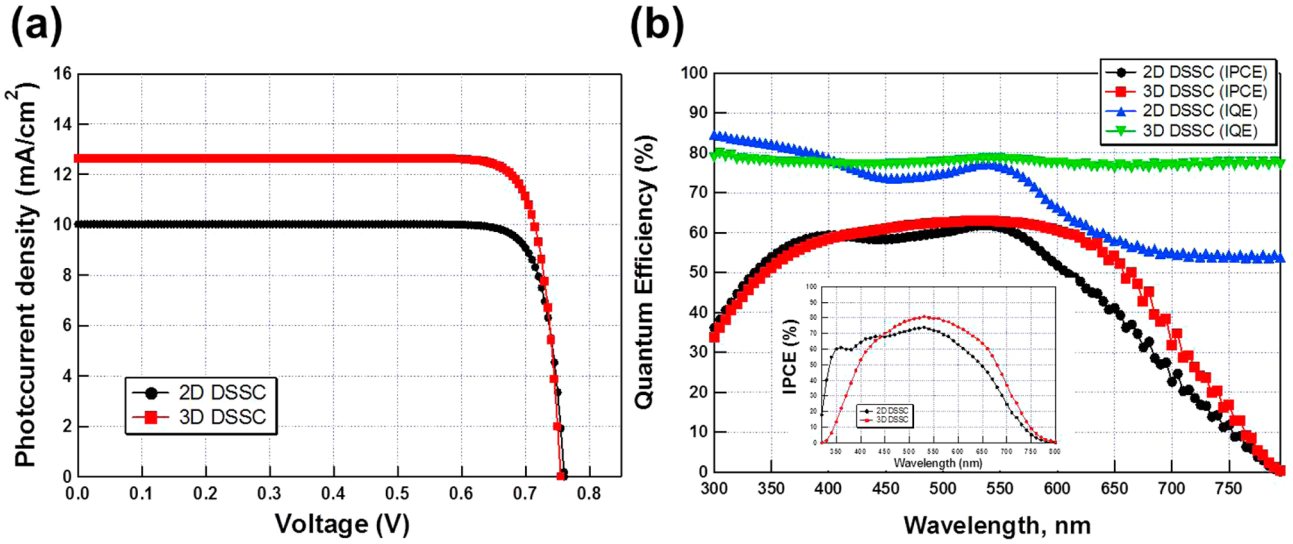

Figure 8. (a) $J-V$ characteristics comparison of the 3D and 2D DSSCs. (b) IPCE and IQE comparisons of the 3D and 2D DSSCs.

electrons only occupy one energy level, i.e., the conduction band of TiO_2, and a first-order recombination. However, we note that the numerical FEM model can easily be expanded to include higher-order recombination. Furthermore, in the model the ionic transport in the electrolyte as well as the series resistance in the contacts are not included. Although in practice this is not the case, these assumptions allow us to compare the effects of charge transport that is purely introduced by the 3D ITO NR electrode, which is the main focus of the work. Figure 7a shows the schematic of the simulation flow, and Figure 7b demonstrates the energy diagram and recombination considered in the model.

Using this model, we calculated the $J-V$ curves, recombination profile, external quantum efficiencies, internal quantum efficiencies, and electron flows of the planar and 3D DSSCs. Figure 8a shows the comparison of the $J-V$ characteristics of the 2D and 3D DSSCs with a photo active layer of 15 μm thick, and ITO NR of 13 μm long with a 1.2 μm pitch size (corresponding to the 15 μm thick DSSC in Table 1). It can be seen that the short circuit current can be improved by about 25%. Compared with the experimental $J-V$ characteristics shown in Figure 5a (curve c and curve f), the simulation is qualitatively consistent with the experimental improvements. Figure 8b shows the quantum efficiency comparisons between the 2D and 3D DSSCs, which elucidates the origin of the short circuit current improvement. It is observed that the internal quantum efficiencies of 3D DSSC is improved almost over the entire spectrum, especially at long wavelengths at which the N719 dye absorbs, and the overall trend of the simulated IPCE spectra matches quite well the shape of the experimental IPCE results using the same geometric dimensions (see Figure 8b inset). The enhancement of IPCE and IQE at the spectral range from 600 to 750 nm has a significant effect on the observed photocurrent improvement, since the photon flux of the solar irradiance spectrum peaks in this wavelength range.

In Figure 9a, we plot the electron concentration and the electron flow directions for both the 3D and 2D DSSCs. It is clear that the electron concentration for the 3D DSSC is more than 1 order of magnitude lower than that of the 2D DSSC case in almost the entire TiO_2 domain, and thus the recombination rates are significantly lower due to the electron concentration-dependent recombination rate, which says $U(\vec{r}) = (n(\vec{r}) - \bar{n})/(\tau)$, where $U(\vec{r})$ is the recombination rate at location $\vec{r}$. The reduced recombination rate can be clearly concluded from Figure 9b, where the recombination rates of both the 3D and 2D DSSCs are drawn in different color scales. We argue here that the higher internal quantum efficiency of the 3D DSSC at long wavelengths observed at Figure 8b is due to the weak absorption efficiency of the N719 dye, which causes a large portion of the photogenerated electrons to distribute at the far end of the TiO_2 active layer from the photoanode. In 2D DSSC, these electrons have to hop over a few microns thick TiO_2 NPs accompanied by a high recombination loss. The ITO NRs provide an excellent pathway, especially for these electrons, and leads to a higher photocurrent. This can be illustrated by the arrows shown in Figure 9a, where the electron flow directions, defined as $\nabla n(\vec{r})$, are plotted. As expected, the ITO NRs act as short pathways for the electrons to reach the

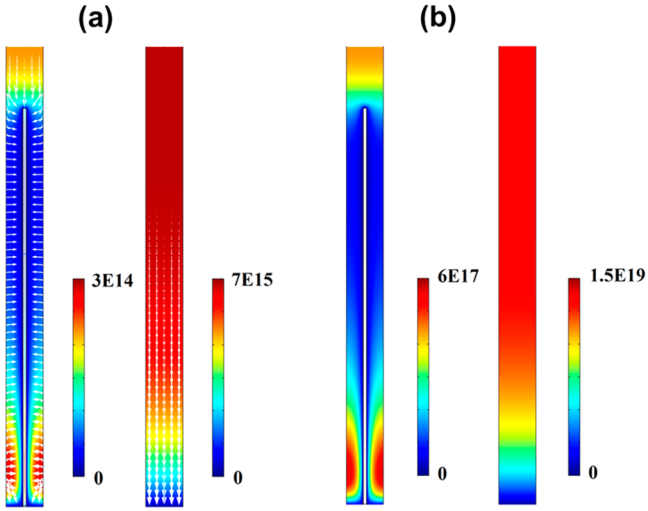

Figure 9. (a) Comparison of the electron concentration (1/cm^3) shown by color plot and electron flow (shown by white arrows) of the 3D and 2D DSSCs at short circuit condition under AM 1.5 illumination; (b) recombination rate comparison of the 3D and 2D DSSCs at short circuit condition under AM 1.5 illumination. (a) and (b) are plotted on log scale.

dx.doi.org/10.1021/am504126g | ACS Appl. Mater. Interfaces 2014, 6, 17713−17722

photoanode and leave the device with less recombination with the electrolyte in comparison with that in the 2D DSSC case.

CONCLUSION

The designed 3D ITO NR structures were employed as efficient pathways for photogenerated electrons for N719-based DSSCs. The use of 3D ITO structure significantly reduces a major energy conversion loss mechanism in DSSC, which is the recombination of the electrons in the TiO_2 conduction band with the redox species in the electrolyte. Compared to a 2D planar DSSC, an energy conversion efficiency enhancement ranging from 10% to 20% has been demonstrated experimentally. An FEM-based simulation model has been developed to elucidate the advantages of the 3D DSSC compared to its 2D counterpart. Similar nanostructure strategies can be applied to a broader class of solar energy conversion devices. This work has demonstrated that, in general, a 3D architecture can be used to decouple the functions of charge transport from photon collection in a solar cell device design.

AUTHOR INFORMATION

Corresponding Author

*E-mail: r-chang@northwestern.edu

Author Contributions

[§]B.L. and P.G. contributed equally.

Notes

The authors declare no competing financial interest.

ACKNOWLEDGMENTS

The experimental part of this work were supported by DOE award No. DE-FG02-08ER46536. Modeling and simulation was supported by DOE award No. DE-SC0001059. The authors would like to acknowledge Dr. Alex B. F. Martinson and Dr. Pierfrancesco Zilio for valuable discussions. This work made use of the EPIC facility (NUANCE Center-Northwestern University), which has received support from the MRSEC program (NSF DMR-1121262) at the Materials Research Center, and the Nanoscale Science and Engineering Center (EEC-0118025/003), both programs of the National Science Foundation, the State of Illinois, and Northwestern University. Use of the Center for Nanoscale Materials (project CNM 32301 and CNM 39151) was supported by the U. S. Department of Energy, Office of Science, Office of Basic Energy Sciences, under Contract No. DE-AC02-06CH11357.

REFERENCES

(1) Chung, I.; Lee, B.; He, J.; Chang, R. P. H.; Kanatzidis, M. G. All-Solid-State Dye-Sensitized Solar Cells with High Efficiency. *Nature* **2012**, *485*, 486−489.

(2) Lee, B.; Buchholz, D. B.; Chang, R. P. H. An All Carbon Counter Electrode for Dye Sensitized Solar Cells. *Energy Environ. Sci.* **2012**, *5*, 6941−6952.

(3) Habas, S. E.; Platt, H. A. S.; van Hest, M. F. A. M.; Ginley, D. S. Low-Cost Inorganic Solar Cells: From Ink To Printed Device. *Chem. Rev.* **2010**, *110*, 6571−6594.

(4) Gratzel, M. Photoelectrochemical Cells. *Nature* **2001**, *414*, 338−344.

(5) Brabec, C. J.; Gowrisanker, S.; Halls, J. J. M.; Laird, D.; Jia, S.; Williams, S. P. Polymer−Fullerene Bulk-Heterojunction Solar Cells. *Adv. Mater.* **2010**, *22*, 3839−3856.

(6) Tang, J.; Sargent, E. H. Infrared Colloidal Quantum Dots for Photovoltaics: Fundamentals and Recent Progress. *Adv. Mater.* **2011**, *23*, 12−29.

(7) Weickert, J.; Dunbar, R. B.; Hesse, H. C.; Wiedemann, W.; Schmidt-Mende, L. Nanostructured Organic and Hybrid Solar Cells. *Adv. Mater.* **2011**, *23*, 1810−1828.

(8) Burschka, J.; Pellet, N.; Moon, S.-J.; Humphry-Baker, R.; Gao, P.; Nazeeruddin, M. K.; Gratzel, M. Sequential Deposition as a Route to High-Performance Perovskite-Sensitized Solar Cells. *Nature* **2013**, *499*, 316−319.

(9) Liu, M.; Johnston, M. B.; Snaith, H. J. Efficient Planar Heterojunction Perovskite Solar Cells by Vapour Deposition. *Nature* **2013**, *501*, 395−398.

(10) Grätzel, M. Solar Energy Conversion by Dye-Sensitized Photovoltaic Cells. *Inorg. Chem.* **2005**, *44*, 6841−6851.

(11) Schlenker, C. W.; Thompson, M. E. The Molecular Nature of Photovoltage Losses in Organic Solar Cells. *Chem. Commun.* **2011**, *47*, 3702−3716.

(12) Lee, B.; Hwang, D.-K.; Guo, P.; Ho, S.-T.; Buchholtz, D. B.; Wang, C.-Y.; Chang, R. P. H. Materials, Interfaces, and Photon Confinement in Dye-Sensitized Solar Cells. *J. Phys. Chem. B* **2010**, *114*, 14582−14591.

(13) Yu, H.; Zhang, S.; Zhao, H.; Zhang, H. Photoelectrochemical Quantification of Electron Transport Resistance of TiO_2 Photoanodes for Dye-Sensitized Solar Cells. *Phys. Chem. Chem. Phys.* **2010**, *12*, 6625−6631.

(14) van Bavel, S.; Sourty, E.; de With, G.; Frolic, K.; Loos, J. Relation between Photoactive Layer Thickness, 3D Morphology, and Device Performance in P3HT/PCBM Bulk-Heterojunction Solar Cells. *Macromolecules* **2009**, *42*, 7396−7403.

(15) Mor, G. K.; Shankar, K.; Paulose, M.; Varghese, O. K.; Grimes, C. A. Use of Highly-Ordered TiO_2 Nanotube Arrays in Dye-Sensitized Solar Cells. *Nano Lett.* **2005**, *6*, 215−218.

(16) Baxter, J. B.; Aydil, E. S. Nanowire-Based Dye-Sensitized Solar Cells. *Appl. Phys. Lett.* **2005**, *86*, 053114.

(17) Martinson, A. B. F.; Elam, J. W.; Hupp, J. T.; Pellin, M. J. ZnO Nanotube Based Dye-Sensitized Solar Cells. *Nano Lett.* **2007**, *7*, 2183−2187.

(18) Richter, C.; Schmuttenmaer, C. A. Exciton-like Trap States Limit Electron Mobility in TiO_2 Nanotubes. *Nat. Nanotechnol.* **2010**, *5*, 769−772.

(19) Martinson, A. B. F.; Elam, J. W.; Liu, J.; Pellin, M. J.; Marks, T. J.; Hupp, J. T. Radial Electron Collection in Dye-Sensitized Solar Cells. *Nano Lett.* **2008**, *8*, 2862−2866.

(20) Tétreault, N.; Arsenault, É.; Heiniger, L.-P.; Soheilnia, N.; Brillet, J.; Moehl, T.; Zakeeruddin, S.; Ozin, G. A.; Grätzel, M. High-Efficiency Dye-Sensitized Solar Cell with Three-Dimensional Photoanode. *Nano Lett.* **2011**, *11*, 4579−4584.

(21) Chappel, S.; Grinis, L.; Ofir, A.; Zaban, A. Extending the Current Collector into the Nanoporous Matrix of Dye Sensitized Electrodes. *J. Phys. Chem. B* **2005**, *109*, 1643−1647.

(22) Alibabaei, L.; Farnum, B. H.; Kalanyan, B.; Brennaman, M. K.; Losego, M. D.; Parsons, G. N.; Meyer, T. J. Atomic Layer Deposition of TiO_2 on Mesoporous nanoITO: Conductive Core−Shell Photoanodes for Dye-Sensitized Solar Cells. *Nano Lett.* **2014**, *14*, 3255−3261.

(23) Wan, Q.; Dattoli, E. N.; Fung, W. Y.; Guo, W.; Chen, Y.; Pan, X.; Lu, W. High-Performance Transparent Conducting Oxide Nanowires. *Nano Lett.* **2006**, *6* (12), 2909−2915.

(24) Lowndes, D. H.; Geohegan, D. B.; Puretzky, A. A.; Norton, D. P.; Rouleau, C. M. Synthesis of Novel Thin-Film Materials by Pulsed Laser Deposition. *Science* **1996**, *273*, 898−903.

(25) Harvey, S. P.; Mason, T. O.; Buchholz, D. B.; Chang, R. P. H.; Körber, C.; Klein, A. Carrier Generation and Inherent Off-Stoichiometry in Zn, Sn Codoped Indium Oxide (ZITO) Bulk and Thin-Film Specimens. *J. Am. Ceram. Soc.* **2008**, *91*, 467−472.

(26) Gao, J.; Chen, R.; Li, D. H.; Jiang, L.; Ye, J. C.; Ma, X. C.; Chen, X. D.; Xiong, Q. H.; Sun, H. D.; Wu, T. UV Light Emitting Transparent Conducting Tin-Doped Indium Oxide (ITO) Nanowires. *Nanotechnology* **2011**, *22*, 195706.

(27) Kim, H.; Horwitz, J. S.; Kushto, G.; Piqué, A.; Kafafi, Z. H.; Gilmore, C. M.; Chrisey, D. B. Effect of Film Thickness on the

Properties of Indium Tin Oxide Thin Films. *J. Appl. Phys.* **2000**, *88*, 6021−6025.
(28) McAlpine, M. C.; Friedman, R. S.; Lieber, C. M. Nanoimprint Lithography for Hybrid Plastic Electronics. *Nano Lett.* **2003**, *3*, 443−445.
(29) Li, S. Q.; Guo, P.; Zhang, L.; Zhou, W.; Odom, T. W.; Seideman, T.; Ketterson, J. B.; Chang, R. P. H. Infrared Plasmonics with Indium-Tin-Oxide Nanorod Arrays. *ACS Nano* **2011**, *5*, 9161−9170.
(30) Ott, A. W.; Chang, R. P. H. Atomic Layer-Controlled Growth of Transparent Conducting ZnO on Plastic Substrates. *Mater. Chem. Phys.* **1999**, *58*, 132−138.
(31) Lee, B.; Buchholz, D. B.; Guo, P.; Hwang, D.-K.; Chang, R. P. H. Optimizing the Performance of a Plastic Dye-Sensitized Solar Cell. *J. Phys. Chem. C* **2011**, *115*, 9787−9796.
(32) Ito, S.; Nazeeruddin, M. K.; Liska, P.; Comte, P.; Charvet, R.; Péchy, P.; Jirousek, M.; Kay, A.; Zakeeruddin, S. M.; Grätzel, M. Photovoltaic Characterization of Dye-Sensitized Solar Cells: Effect of Device Masking on Conversion Efficiency. *Prog. Photovoltaics* **2006**, *14*, 589−601.
(33) Kroon, J. M.; Bakker, N. J.; Smit, H. J. P.; Liska, P.; Thampi, K. R.; Wang, P.; Zakeeruddin, S. M.; Grätzel, M.; Hinsch, A.; Hore, S.; Würfel, U.; Sastrawan, R.; Durrant, J. R.; Palomares, E.; Pettersson, H.; Gruszecki, T.; Walter, J.; Skupien, K.; Tulloch, G. E. Nanocrystalline Dye-Sensitized Solar Cells having Maximum Performance. *Prog. Photovoltaics* **2007**, *15*, 1−18.
(34) Zhu, K.; Neale, N. R.; Miedaner, A.; Frank, A. J. Enhanced Charge-Collection Efficiencies and Light Scattering in Dye-Sensitized Solar Cells Using Oriented TiO_2 Nanotubes Arrays. *Nano Lett.* **2006**, *7*, 69−74.
(35) Lee, B. H.; Song, M. Y.; Jang, S.-Y.; Jo, S. M.; Kwak, S.-Y.; Kim, D. Y. Charge Transport Characteristics of High Efficiency Dye-Sensitized Solar Cells Based on Electrospun TiO_2 Nanorod Photoelectrodes. *J. Phys. Chem. C* **2009**, *113*, 21453−21457.
(36) Yella, A.; Lee, H.-W.; Tsao, H. N.; Yi, C.; Chandiran, A. K.; Nazeeruddin, M. K.; Diau, E. W.-G.; Yeh, C.-Y.; Zakeeruddin, S. M.; Grätzel, M. Porphyrin-Sensitized Solar Cells with Cobalt (II/III)-Based Redox Electrolyte Exceed 12% Efficiency. *Science* **2011**, *334*, 629−634.
(37) Soedergren, S.; Hagfeldt, A.; Olsson, J.; Lindquist, S.-E. Theoretical Models for the Action Spectrum and the Current−Voltage Characteristics of Microporous Semiconductor Films in Photoelectrochemical Cells. *J. Phys. Chem.* **1994**, *98*, 5552−5556.
(38) Martinson, A. B. F.; Hamann, T. W.; Pellin, M. J.; Hupp, J. T. New Architectures for Dye-Sensitized Solar Cells. *Chem.—Eur. J.* **2008**, *14*, 4458−4467.
(39) Bruggeman, D. A. G. Berechnung verschiedener physikalischer Konstanten von heterogenen Substanzen. I. Dielektrizitätskonstanten und Leitfähigkeiten der Mischkörper aus isotropen Substanzen [Calculation of various physical constants of heterogeneous substances. II. Dielectric constant and conductivity of polycrystals of nonregular systems]. *Ann. Phys.* **1935**, *416*, 636−664.
(40) Wenger, S.; Schmid, M.; Rothenberger, G.; Gentsch, A.; Grätzel, M.; Schumacher, J. r. O. Coupled Optical and Electronic Modeling of Dye-Sensitized Solar Cells for Steady-State Parameter Extraction. *J. Phys. Chem. C* **2011**, *115*, 10218−10229.
(41) Rothenberger, G.; Comte, P.; Grätzel, M. A Contribution to the Optical Design of Dye-Sensitized Nanocrystalline Solar Cells. *Sol. Energy Mater. Sol. Cells* **1999**, *58*, 321−336.
(42) Palik, E. D. *Handbook of Optical Constants of Solids*; Academic Press: San Diego, 1985.
(43) Paulson, P. D.; Hegedus, S. S. Accurate Determination of Optical Constants of Textured SnO_2 Using Low Incidence Angle Spectroscopic Ellipsometry. *J. Appl. Phys.* **2004**, *96*, 5469−5477.
(44) Li, S.-Q.; Guo, P.; Buchholz, D. B.; Zhou, W.; Hua, Y.; Odom, T. W.; Ketterson, J. B.; Ocola, L. E.; Sakoda, K.; Chang, R. P. H. Plasmonic−Photonic Mode Coupling in Indium-Tin-Oxide Nanorod Arrays. *ACS Photonics* **2014**, *1*, 163−172.
(45) Centurioni, E. Generalized Matrix Method for Calculation of Internal Light Energy Flux in Mixed Coherent and Incoherent Multilayers. *Appl. Opt.* **2005**, *44*, 7532−7539.
(46) Peter, L. M. Characterization and Modeling of Dye-Sensitized Solar Cells. *J. Phys. Chem. C* **2007**, *111*, 6601−6612.
(47) Zhu, K.; Kopidakis, N.; Neale, N. R.; van de Lagemaat, J.; Frank, A. J. Influence of Surface Area on Charge Transport and Recombination in Dye-Sensitized TiO_2 Solar Cells. *J. Phys. Chem. B* **2006**, *110*, 25174−25180.
(48) Bisquert, J.; Zaban, A.; Greenshtein, M.; Mora-Seró, I. Determination of Rate Constants for Charge Transfer and the Distribution of Semiconductor and Electrolyte Electronic Energy Levels in Dye-Sensitized Solar Cells by Open-Circuit Photovoltage Decay Method. *J. Am. Chem. Soc.* **2004**, *126*, 13550−13559.
(49) Barnes, P. R. F.; Anderson, A. Y.; Koops, S. E.; Durrant, J. R.; O'Regan, B. C. Electron Injection Efficiency and Diffusion Length in Dye-Sensitized Solar Cells Derived from Incident Photon Conversion Efficiency Measurements. *J. Phys. Chem. C* **2008**, *113*, 1126−1136.
(50) Gonzalez-Vazquez, J. P.; Anta, J. A.; Bisquert, J. Determination of the Electron Diffusion Length in Dye-Sensitized Solar Cells by Random Walk Simulation: Compensation Effects and Voltage Dependence. *J. Phys. Chem. C* **2010**, *114*, 8552−8558.